Research Square

Preprints are preliminary reports that have not undergone peer review.
They should not be considered conclusive, used to inform clinical practice,
or referenced by the media as validated information.

Multi-layer spatial profiling reveals early response-associated immune remodeling after one cycle of neoadjuvant combination therapy in triple-negative breast cancer

Jiao-mei Yuan
South China University of Technology, Guangzhou University Town
Fei Ji
Guangdong Academy of Medical Sciences
Kun Wang
gzwangkun@126.com

Guangdong Academy of Medical Sciences

Article

Keywords: triple-negative breast cancer, neoadjuvant therapy, multiplex immunofluorescence, tumour immune microenvironment, spatial analysis, pathological complete response

Posted Date: November 18th, 2026

DOI: https://doi.org/10.21203/rs.3.rs-11231201/v1

License: This work is licensed under a Creative Commons Attribution 4.0 International License.
Read Full License

Additional Declarations: No competing interests reported.

Abstract

Background

Early identification of response to neoadjuvant therapy remains challenging in triple-negative breast cancer (TNBC), and conventional cell-density measurements may not fully capture treatment-induced changes in the spatial organisation of the tumour immune microenvironment. We investigated whether early spatial remodelling after a single treatment cycle was associated with subsequent pathological response.

Methods

This retrospective translational analysis used prospectively collected matched pre-treatment and post-cycle-1 core-needle biopsies from ten TNBC patients (five pCR and five non-pCR) enrolled in a clinical trial of neoadjuvant sintilimab, anlotinib and sequential chemotherapy. Six-colour multiplex immunofluorescence (CD8, CD20, CD68, FOXP3, PANCK and DAPI) was applied, and more than 1.7 million single cells were evaluated using a four-tier spatial framework comprising immune-cell density, tumour–immune spatial co-localisation, immune hotspot organisation and within-hotspot cellular interactions.

Results

After one treatment cycle, intratumoral and stromal CD8 + T-cell densities increased, whereas intratumoral CD68 + macrophages and stromal FOXP3 + regulatory T cells decreased. Tumour–CD20 + B-cell spatial co-localisation increased at the raw P-value level but did not survive FDR correction. The intratumoral immune hotspot score (Sintra/immune) decreased predominantly in patients who subsequently achieved pCR, and post-treatment values differed between pCR and non-pCR groups at the raw P-value level ($P = 0.032$; $q = 0.064$; exploratory ROC AUC = 0.92, 95% CI 0.66–1.00). Within immune hotspots, intratumoral CD68+–FOXP3 + interactions decreased and CD20+–CD8 + interactions increased across the cohort (both $q < 0.05$). Peritumoral CD20+–FOXP3 + interaction changes also differed between response groups ($P = 0.032$), although this association did not survive FDR correction.

Conclusions

These findings identify rapid spatial reorganisation of the TNBC immune microenvironment after a single treatment cycle and exploratory hotspot-level features associated with subsequent pathological response. Larger prospective cohorts are required for validation.

Background

Triple-negative breast cancer (TNBC), defined by the absence of oestrogen receptor, progesterone receptor, and HER2 overexpression, accounts for approximately 15–20% of breast cancers and carries an aggressive clinical course with limited targeted treatment options [1–3]. The addition of immune checkpoint blockade to neoadjuvant chemotherapy has improved pathological complete response (pCR) and event-free survival in high-risk early-stage TNBC [4–7]. Yet a substantial proportion of patients still fail to achieve pCR, and baseline immune biomarkers incompletely capture the heterogeneity of treatment response [8, 9]. By the time response is assessed at surgery, the opportunity for early treatment adaptation has already passed.

Spatial organisation, rather than immune cell abundance alone, increasingly appears to govern response: local lymphocyte aggregates, tumour–immune interfaces, and the compartment in which immune cells reside all carry prognostic information that bulk density misses [10–12]. At the same time, the immune microenvironment reorganises rapidly under therapy. Imaging mass cytometry of the NeoTRIP trial showed that combining baseline with early on-treatment tissue features substantially improved prediction of immunotherapy response over baseline alone [13]. These two threads converge on a specific possibility: that the spatial architecture of the TNBC microenvironment after only one cycle of treatment may carry information that neither baseline tissue nor late surgical tissue can provide.

Whether such cycle-one spatial reorganisation can be captured in a workflow that is deployable in routine pathology, rather than in specialised imaging mass cytometry or 40-marker MIBI panels [13–16], has not been established. Prior mIF studies have demonstrated the feasibility of quantifying treatment-related immune changes in breast cancer, including paired pre-treatment biopsies and post-treatment tumour resections [18], while high-dimensional spatial studies have profiled on-treatment tissue using platforms that are not yet practical for routine deployment [13, 15]. Whether a six-colour mIF panel, within reach of tertiary pathology laboratories, can detect cycle-one spatial features associated with subsequent pathological response therefore remains an open question.

Here we apply a four-tier spatial framework — cell density, tumour–immune co-localisation, immune hotspot organisation, and within-hotspot cellular interactions — to matched pre-treatment and post-cycle-1 core-needle biopsies from ten TNBC patients receiving neoadjuvant sintilimab, anlotinib and chemotherapy. We ask whether each tier captures information that the others do not, and whether any of them captures a cycle-1 spatial feature associated with subsequent pathological response.

Methods

Patient cohort and study design

This retrospective translational analysis included prospectively collected longitudinal specimens from ten women with histologically confirmed invasive triple-negative breast cancer (TNBC; ER−/PR−/HER2−), clinical stage IIA–IIIB (cT1–T4, cN0–2, M0), who had been enrolled in the prospective phase II NeoSACT trial (ClinicalTrials.gov identifier: NCT04877821; first submitted on 30 April 2021 and first posted on 7

May 2021). All patients received neoadjuvant therapy in 21-day cycles comprising three concurrent components: (i) sintilimab (anti-PD-1, 200 mg intravenously on day 1 of each cycle); (ii) anlotinib (a multi-target tyrosine kinase inhibitor with activity against VEGFR, PDGFR and FGFR; 12 mg orally once daily on days 1–14 of each cycle); and (iii) sequential chemotherapy consisting of nab-paclitaxel plus carboplatin for cycles 1–4, followed by epirubicin plus cyclophosphamide for cycles 5–8. For brevity, this three-component regimen is hereafter referred to as neoadjuvant combination therapy.

As part of the parent clinical trial, vacuum-assisted core-needle biopsy specimens (Mammotome system) were prospectively collected at two time points: (i) before treatment initiation (pre-treatment, baseline) and (ii) at the end of cycle 1, immediately before cycle 2 (post-cycle-1, C1), yielding twenty FFPE specimens in total. Both baseline and post-cycle-1 biopsies were therefore obtained during the nab-paclitaxel/carboplatin phase of treatment. At the time of the post-cycle-1 biopsy, surgical pathological response was not yet known.

Following completion of neoadjuvant therapy, all patients underwent surgery. Pathological complete response (pCR) was defined as ypT0/is ypN0 on surgical pathology. Five patients achieved pCR and five had residual invasive disease (non-pCR). Baseline clinicopathological characteristics are summarised in Supplementary Table S1.

The parent NeoSACT trial was approved by the Research Ethics Committee of Guangdong General Hospital, Guangdong Academy of Medical Sciences (approval no. KY-Z-2021-511-01). All participants provided written informed consent for trial participation and the use of collected biospecimens for research in accordance with the Declaration of Helsinki.

Multiplex immunofluorescence staining and single-cell phenotyping

FFPE tissue sections (4 μm) from all twenty specimens were stained using a six-colour mIF panel comprising five immune and tumour cell markers — CD8 (cytotoxic T cells), CD20 (B cells), CD68 (macrophages), FOXP3 (regulatory T cells), and pan-cytokeratin (PANCK; tumour cells) — together with DAPI for nuclear counterstaining and cell segmentation. Antibody clones, vendors, catalogue numbers, and dilutions are listed in Supplementary Table S6. Staining was performed by Panovue Biological Technology Co., Ltd. (Beijing, China) following validated multiplex IHC/IF protocols consistent with published best-practice guidelines [29]. Whole-slide images were acquired and subsequently imported into HALO image analysis software (v3.5, Indica Labs, Albuquerque, NM, USA) for automated cell segmentation, single-cell phenotyping, and tumour nest versus stromal compartment classification. Each nucleus was classified into one of the five phenotypes based on marker expression; tumour nest and stromal compartments were delineated using the PANCK signal via a HALO tissue classifier. A total of 1,708,867 cells were identified across twenty specimens (range: 3,757–522,597 per specimen, reflecting variability in core-needle biopsy specimen size).

Immune cell density analysis

Immune cell densities were quantified as the number of phenotype-positive cells per mm² within the tumour nest and stromal compartments separately, using the HALO-derived single-cell phenotype assignments and tissue classifier outputs. Pre- versus post-treatment comparisons within each compartment and cell type were assessed using the two-sided Wilcoxon signed-rank test on paired per-patient densities.

Bivariate pair correlation function analysis

Spatial co-localisation was assessed using the bivariate cross-PCF g(r) computed at r = 10–300 μm with step size 10 μm, following Nawaz et al. [11] Density estimation used a second-order Epanechnikov kernel with bandwidth 10 μm, chosen to balance bias-variance trade-off given the mean nearest-neighbour spacing of ~ 15–25 μm between phenotype-defined cell populations in TNBC biopsy specimens, and to maintain smoothness of g(r) estimates in a small-sample context. To ensure robustness, sensitivity analyses were performed at bandwidths of 15 and 20 μm; all qualitative conclusions were preserved (Supplementary Table S2). Complete spatial randomness (CSR) envelopes (2.5–97.5% range) were estimated via 99 toroidal shift permutations of the reference cell population, following the convention applied by Nawaz et al. [11]. Analyses of PANCK+ reference populations exceeding 5,000 cells were run on random subsamples of 5,000 cells, with the random seed fixed per patient for reproducibility. To assess stability under subsampling, we repeated the entire pipeline with 10 independent seed series: paired Cohen's d values remained tightly clustered (PANCK–CD8: range + 0.52 to + 0.55; PANCK–CD20: range + 0.69 to + 0.75), confirming that point estimates are robust to the specific subsample (Supplementary Table S3). Eight cell pairs were analysed (four PANCK–immune, four immune–immune); g(r) at r = 50 μm was pre-specified as the primary summary statistic (corresponding to ~ 2–3 typical cell diameters in breast tissue), with r = 20 μm and r = 30 μm evaluated as additional spatial scales (Supplementary Table S2). Pre- versus post-treatment comparisons used the two-sided Wilcoxon signed-rank test on paired per-patient g(50) values.

Getis-Ord G* immune hotspot analysis

Spatial hotspot analysis was performed on whole-slide single-cell maps using 50 × 50 μm² grids (corresponding to ~ 2–3 typical cell diameters in breast tissue) and fourth-order neighbourhood weighting, following the approach of Nawaz et al. and Zhang et al. [11, 23]. The Getis-Ord G* statistic was calculated independently for total immune cells and for tumour cells (PANCK+) within each grid cell. Grid cells were classified as intratumoral immune hotspots (IH_{intra}) when both immune and tumour cell enrichment were statistically significant ($P < 0.05$; classification performed without further multiple-testing correction within slides, consistent with the original framework of Nawaz et al. [11]), as peritumoral immune hotspots (IH_{peri}) when only immune enrichment was significant, and as cancer hotspots when only tumour enrichment was significant. The intratumoral immune hotspot score

Sintra/immune was defined as IH_{intra} / (IH_{intra} + IH_{peri}) [11, 23]. Mean cell count per 50 × 50 μm² grid within IH_{intra} and IH_{peri} was calculated for each immune cell type to enable compartment-resolved density comparisons.

Delaunay triangulation-based cellular interaction analysis

Cellular interaction analysis within immune hotspots was performed following the approach of Zhang et al. [23], computing Delaunay triangulation independently for each individual immune hotspot. For each sample and each compartment (IH_{intra} or IH_{peri}), cells of the four immune phenotypes (CD8+, CD20+, CD68+, FOXP3+) within each individual hotspot were used to build a Delaunay graph, with edges exceeding 250 μm excluded following Zhang et al. [23]. PANCK+ tumour cells were excluded from the network. Individual hotspots containing fewer than four immune cells were excluded from triangulation to ensure each Delaunay graph contained at least one valid triangle. Interaction frequency for each cell-type pair within each hotspot was defined as the number of edges connecting that pair divided by the total number of retained edges within the hotspot. A sample-level interaction frequency was then computed as the simple arithmetic mean of per-hotspot frequencies across all qualifying hotspots within the compartment. Across the cohort, 381 of 467 individual hotspots met the minimum-cell criterion and contributed to the aggregation. This aggregation gives equal weight to each qualifying hotspot when deriving a patient-level summary; the patient, rather than the individual hotspot, remained the inferential unit for all subsequent statistical comparisons.

Statistics and reproducibility

Spatial statistical analyses, including cross-PCF computation, Getis-Ord G* hotspot classification, Delaunay triangulation-based interaction analysis, and all downstream group comparisons, were implemented using custom scripts in R. Pre- versus post-treatment comparisons and intra- versus peri-tumoral comparisons within the same patient were assessed using the two-sided Wilcoxon signed-rank test (paired). Between-group comparisons (pCR vs. non-pCR), both at single time points and for within-patient pre→post changes (Δ), were performed using the two-sided Mann–Whitney U test. Effect size was estimated using Cohen's d (paired formula for paired comparisons; pooled-SD formula for unpaired comparisons). Given the exploratory, hypothesis-generating nature of the study, raw P values are reported together with effect sizes (Cohen's d) and, where informative, direction-of-effect counts (e.g., post > pre in n/10 patients). To account for multiple comparisons while preserving the prespecified multi-layer structure, Benjamini–Hochberg false discovery rate (BH-FDR) correction was applied separately within each analytical tier (Tier 1: density; Tier 2: cross-PCF; Tier 3: hotspot compartment analyses; Tier 4: Delaunay interactions). For Tier 4, BH-FDR was applied jointly across 24 tests comprising 12 pre→post paired comparisons and 12 Δ pCR-versus-non-pCR comparisons. Raw and BH-adjusted P values for the complete set of 48 tests are provided in Supplementary Table S4. Results with $q < 0.05$ were considered robust to the specified within-tier multiplicity correction; findings with raw $P < 0.05$ but $q \geq 0.05$ were treated as exploratory. For the two-sided Wilcoxon signed-rank test with n = 5 paired observations, the

theoretical minimum attainable P value is 2/32 = 0.0625, reflecting the discreteness of the test statistic in small samples; in such cases, interpretation emphasised effect size (Cohen's d) and direction-of-effect counts alongside the exact P value. Exploratory ROC analysis was performed for post-treatment Sintra/immune in relation to pCR status in R. The AUC was reported with a 95% confidence interval estimated by non-parametric bootstrap resampling (1,000 iterations). Given the limited sample size, no clinically actionable cutoff was prespecified or inferred.

Results

Patient characteristics and single-cell phenotyping

We profiled twenty matched pre- and post-cycle-1 core-needle biopsies from ten patients with stage IIA–IIIB TNBC (five who subsequently achieved pCR, five who did not), yielding 1,708,867 segmented cells across the cohort (median 84,791 per specimen; range 3,757–522,597). Baseline clinicopathological characteristics are summarised in Supplementary Table S1. Baseline stromal CD8 + and CD20 + densities (median 14.8 and 459 cells/mm²) fell within the range previously reported for treatment-naive TNBC core-needle biopsies [14, 17, 18]. All downstream analyses used cell density per mm² of tissue area to control for variability in biopsy size.

Cycle-one combination therapy is associated with coordinated immune-cell density changes

A single cycle of combination therapy was associated with coordinated changes in immune cell composition. The most pronounced change was a sevenfold rise in intratumoral CD8 + T cell density (median 2.0 → 13.9 cells/mm², P = 0.002, q = 0.016, Cohen's d = + 0.83), accompanied by a more than fourfold increase in stromal CD8 + T cells (14.8 → 65.0 cells/mm², P = 0.037, d = + 0.93). Intratumoral CD68 + macrophages decreased 2.6-fold (175.7 → 67.4 cells/mm², P = 0.027, d = − 0.85), while stromal FOXP3 + regulatory T cells decreased 1.6-fold (173.5 → 106.1 cells/mm², P = 0.027, d = − 0.82). By contrast, CD20 + B cells in either compartment, stromal CD68 + macrophages, and intratumoral FOXP3 + Tregs showed no significant change (Table 1, Fig. 1).

Table 1
Immune cell density before and after neoadjuvant combination therapy.

Compartment	Cell type	Pre-treatment	Post-treatment (C1)	P value	Cohen's d
		Median (IQR)	Median (IQR)		
Tumour	CD8+	2.0 (0.5–4.4)	13.9 (6.1–33.0)	**0.002**	+ 0.83
	CD20+	38.0 (12.6–122.2)	105.0 (15.1–272.6)	0.105	+ 0.62
	CD68+	175.7 (61.3–272.6)	67.4 (53.3–97.6)	**0.027**	−0.85
	FOXP3+	25.0 (8.8–41.5)	24.4 (4.4–45.9)	1.000	+ 0.02
Stroma	CD8+	14.8 (6.3–31.5)	65.0 (27.2–89.7)	**0.037**	+ 0.93
	CD20+	459.0 (288.2–512.7)	487.1 (155.4–697.3)	0.625	+ 0.23
	CD68+	703.3 (467.5–1121.4)	590.4 (182.5–837.4)	0.160	−0.48
	FOXP3+	173.5 (120.5–207.7)	106.1 (49.6–201.2)	**0.027**	−0.82

Values are median (IQR). Bold P values indicate P < 0.05. Two-sided Wilcoxon signed-rank test (paired, n = 10). Densities are in cells/mm².

After Benjamini–Hochberg FDR correction across all eight Tier 1 tests, the intratumoral CD8 + T cell increase remained statistically significant (q = 0.016), while the other three changes did not formally survive the q < 0.05 threshold (q = 0.072 for intratumoral CD68 + macrophages and stromal FOXP3 + Tregs; q = 0.074 for stromal CD8 + T cells). The concordant directions and large effect sizes of these changes (|d| = 0.82–0.93) describe a coordinated early shift in immune-cell composition, with the multiple-testing-robust signal centred on intratumoral CD8 + T cell infiltration.

Cycle-one treatment is associated with increased tumour–CD20 + B-cell spatial co-localisation

Beyond density changes, we next assessed whether treatment altered the spatial relationship between immune and tumour cells, computing bivariate cross-pair correlation functions (cross-PCFs) for all four tumour–immune and four immune–immune cell pairs. The cross-PCF g(r) quantifies the relative co-localisation of two cell types at separation distance r, with values exceeding the complete spatial randomness (CSR) envelope (95% range under random placement) indicating non-random co-localisation.

The largest treatment-associated change was observed for tumour–B cell co-localisation, which increased at r = 50 μm (median g(50) 1.47 → 3.61, raw P = 0.037, Cohen's d = + 0.71). This effect was robust to variation in kernel bandwidth and subsampling seed (Supplementary Tables S2–S3). Tumour–CD8 + T cell co-localisation showed a directionally consistent but weaker trend (P = 0.105, d = + 0.53), whereas the remaining six pairs — including all macrophage- and regulatory T cell-involving relationships — showed no comparable pre- versus post-treatment difference at this scale. After Benjamini–Hochberg correction across the eight tests, no pair survived the q < 0.05 threshold (lowest q = 0.296 for PANCK+–CD20+).

These findings indicate that one cycle of neoadjuvant combination therapy was associated with increased tumour-proximal localisation of CD20 + B cells and, to a lesser extent, CD8 + T cells; however, the tumour–CD20 + finding did not remain significant after correction for multiple testing (Fig. 2a, b).

Cycle-one hotspot architecture differs according to subsequent pathological response

Immune hotspots were classified as intratumoral (IH_{intra}; co-enrichment of immune and PANCK+ tumour cells) or peritumoral (IH_{peri}; immune-cell enrichment without tumour-cell enrichment), following Zhang et al. [23]. The intratumoral immune hotspot score was defined as Sintra/immune = IH_{intra} / (IH_{intra} + IH_{peri}). Baseline Sintra/immune was similar between pCR and non-pCR groups (0.898 vs. 0.897, P = 1.000). In contrast, post-treatment Sintra/immune was lower in pCR patients than in non-pCR patients (0.251 vs. 0.869, raw P = 0.032, BH-FDR q = 0.064, Cohen’s d = − 1.56). Stratified paired analysis further described the source of this divergence: pCR patients showed a large within-group decrease in Sintra/immune after one cycle (median 0.898 → 0.251, Cohen’s d = − 1.68; P = 0.063, the theoretical lower bound of the two-sided Wilcoxon signed-rank test for n = 5 pairs, Pmin = 2/32 = 0.0625; BH-FDR q = 0.084), whereas non-pCR patients showed little change (0.897 → 0.869, Cohen’s d = − 0.34, P = 0.813). Thus, the response groups showed different post-treatment hotspot architectures within 21 days despite similar baseline values, although the between-group comparison did not meet the q < 0.05 threshold after FDR correction (Fig. 3, Table 2).

Table 2
Intratumoral immune hotspot score (Sintra/immune) comparisons.

Comparison	Test	Group 1	Group 2	P value	Cohen's d
		Median [IQR]	Median [IQR]		
pCR: pre vs post	Wilcoxon	0.898 [0.825–0.906]	0.251 [0.203–0.374]	0.063	−1.68
non-pCR: pre vs post	Wilcoxon	0.897 [0.840–0.901]	0.869 [0.850–0.920]	0.813	−0.34
Pre: pCR vs non-pCR	Mann–Whitney	0.898 [0.825–0.906]	0.897 [0.840–0.901]	1.000	−0.30
Post: pCR vs non-pCR	Mann–Whitney	0.251 [0.203–0.374]	0.869 [0.850–0.920]	**0.032**	−1.56

Values are median [IQR]. Bold P values indicate P < 0.05. Statistical tests are listed in the 'Test' column.

To further describe the separation of response groups by post-treatment Sintra/immune, we performed exploratory receiver operating characteristic (ROC) analysis. Post-treatment Sintra/immune yielded an AUC of 0.92 (95% bootstrap CI, 0.66–1.00), consistent with substantial separation between pCR and non-pCR patients in this exploratory cohort. Given the small sample size and absence of an independent validation cohort, this analysis was considered descriptive and hypothesis-generating rather than a validated assessment of predictive performance (Fig. 3b).

Baseline hotspot compartment differences are no longer statistically evident after cycle-one treatment

At baseline, CD20 + B cells (P = 0.004, q = 0.032) and CD68 + macrophages (P = 0.014, q = 0.053) were more abundant in IH_{peri} than in IH_{intra}; after FDR correction, this compartment difference remained significant for CD20 + B cells but not for CD68 + macrophages. After one treatment cycle, no IHi_{ntra}-versus-IH_{peri} comparison reached P < 0.05. Within IH_{peri}, CD20 + B-cell and FOXP3 + Treg densities decreased from pre- to post-treatment (raw P = 0.049 and P = 0.020, respectively), while intratumoral CD8 + T-cell density showed a directional increase (P = 0.064; Fig. 4). These findings indicate that the baseline compartmental pattern was no longer statistically evident after one cycle of combination therapy.

Cycle-one treatment reorganises immune interactions within hotspots

Within-hotspot Delaunay triangulation identified two coordinated treatment-induced interaction changes, both observed across the full cohort. IH_{intra} CD68+–FOXP3 + interaction frequency decreased in 10 of 10

patients (median 0.124 → 0.057, P = 0.002, q = 0.048, Cohen's d = − 1.47), and IH_{intra} CD20+–CD8 + interaction frequency increased in 9 of 10 patients (0.013 → 0.037, P = 0.004, q = 0.048, d = + 0.92). Both effects survived BH-FDR correction across the 24-test Tier 4 family, making these the most robust within-hotspot interaction findings in the dataset. The same directional changes were apparent in IH_{peri} (CD68+–FOXP3 + decrease, raw P = 0.049, q = 0.294, d = − 0.76; CD20+–CD8 + increase, P = 0.084, d = + 0.64), although neither survived BH-FDR correction. No other pair × compartment comparison reached P < 0.05 at the cohort level (Supplementary Table S5A, Fig. 5a, d, e).

Peritumoral FOXP3 + interaction changes show an exploratory association with pathological response

Beyond cohort-wide changes, we examined whether the magnitude of any interaction change differed between response groups by comparing within-patient Δ (post − pre) for all 12 pair × compartment combinations using the Mann–Whitney U test. The most pronounced between-group difference was observed in the IH_{peri} compartment for FOXP3 + Treg-involving interactions. IH_{peri} CD20+–FOXP3 + interaction frequency decreased in 4 of 5 pCR patients (median Δ = −3.3 pp) but increased in 4 of 5 non-pCR patients (median Δ = +2.7 pp). The between-group difference was significant (P = 0.032, Cohen's d = − 1.76; Fig. 5b, f). This was the only Δ comparison reaching raw P < 0.05 across the 12 tests; it did not survive tier-specific BH-FDR correction (q = 0.256) and is reported as hypothesis-generating.

Two additional observations were directionally consistent with differential FOXP3 + interaction reorganisation. First, IH_{peri} CD8+–FOXP3 + Δ followed the same direction with a large effect size (d = − 1.39, P = 0.151). Second, all three IH_{peri} FOXP3+-involving pairs were lower in post-treatment pCR samples than in non-pCR samples, each with large effect sizes (|d| = 1.14–1.28; Supplementary Table S5C, Fig. 5c). IH_{peri} CD20+–CD8 + interaction frequency was also higher in pCR than in non-pCR patients after treatment (P = 0.056, d = + 1.16). These exploratory observations were directionally consistent with lower peritumoral FOXP3 + Treg engagement and greater B cell–CD8 + T cell engagement in pCR patients, but they should not be interpreted as independently significant response-associated findings.

Discussion

A single cycle of neoadjuvant combination therapy was associated with multi-layer spatial reorganisation of the TNBC immune microenvironment. Immune-cell density changes (Tier 1), tumour–immune spatial association (Tier 2), immune hotspot organisation (Tier 3), and within-hotspot cellular interactions (Tier 4) together describe the integrated early effect of cycle-one combination therapy on the tumour microenvironment. Within this multi-layer analysis, post-treatment Sintra/immune differed between response groups at the raw P-value level, although the association did not remain significant after FDR correction (q = 0.064). A pattern of reduced peritumoral FOXP3 + Treg interactions in pCR patients provided additional directional support but likewise did not survive FDR correction and is considered hypothesis-generating.

CD8 + T cell density increased across both tumour nest and stroma, while CD68 + macrophages were specifically reduced in the tumour nest and FOXP3 + regulatory T cells were reduced in the stroma. This compartment-specific pattern of cytotoxic infiltration coupled with immunosuppressive cell depletion is consistent with a coordinated disruption of spatially distinct suppressive niches and is broadly concordant with prior mIF-based monitoring of neoadjuvant breast cancer [18].

The cross-PCF analysis refined this picture by showing that cycle-one therapy preferentially enhanced spatial association of CD20 + B cells with tumour cells, with a directionally consistent trend for CD8 + T cells. The B cell rapprochement is of particular interest because B cells can contribute to anti-tumour immunity and participate in spatially organised immune niches, including tertiary lymphoid structures (TLS) [19–22]. Their spatial convergence towards tumour cells after one treatment cycle may therefore reflect the emergence of spatially organised B-cell-rich immune niches, a feature associated with TLS-related antitumour immunity and immunotherapy response [19–22]. However, TLS were not directly identified by the present six-colour panel.

Tier 3 analyses revealed two complementary aspects of hotspot-level reorganisation. At baseline, CD20 + B cells were more abundant in IH_{peri} than in IH_{intra} after FDR correction ($q = 0.032$), whereas the corresponding CD68 + macrophage difference did not meet the $q < 0.05$ threshold ($q = 0.053$). After one treatment cycle, the baseline compartmental pattern was no longer statistically evident, with decreases in CD20 + B-cell and FOXP3 + Treg density within IH_{peri} and a directional increase in CD8 + T cells within IH_{intra}. In parallel, hotspot architecture differed between response groups after treatment: pCR patients showed lower post-treatment Sintra/immune values than non-pCR patients at the raw P-value level, although this comparison did not survive FDR correction ($q = 0.064$).

Together, these observations are consistent with early treatment-associated reorganisation of immune-cell distribution across tumour-cell-enriched and tumour-cell-nonenriched hotspot compartments, including reduced FOXP3 + Treg representation in IH_{peri} and increased CD8 + T-cell infiltration in the tumour nest. These findings are compatible with established roles of macrophages and regulatory T cells in restricting antitumour T-cell activity [24–27, 30], but whether the observed spatial changes reflect causal disruption of T-cell exclusion requires validation using expanded functional marker panels. The response-associated hotspot pattern also requires validation in larger cohorts.

Two robust within-hotspot interaction changes emerged from the cohort-wide analysis, with notably different compartmental distributions. CD68+–FOXP3 + interaction frequency decreased within both IH_{intra} and IH_{peri}, indicating a broadly distributed weakening of the TAM–Treg spatial pairing. This is biologically consistent with the established TAM–Treg axis, whereby tumour-associated macrophages can promote Treg recruitment and immunosuppressive activity through chemokine- and cytokine-mediated mechanisms [24–27]. The within-hotspot pairing reduction provides a spatial correlate of the parallel density-level decreases of CD68 + macrophages in the tumour nest and FOXP3 + Tregs in the stroma. In contrast, the CD20+–CD8 + interaction increase was observed only within IH_{intra} (Fig. 5e) and was not paralleled by a global slide-level CD20+–CD8 + co-localisation change in cross-PCF, suggesting

that B cell–CD8 + T cell cooperation after cycle-one therapy is a spatially focal phenomenon localised to intratumoral immune hotspots rather than a global redistribution. This focal pattern is consistent with prior work linking localised B-cell-rich immune niches and TLS with coordinated B- and T-cell antitumour immunity [19–22]. Because this analysis combines both response groups, these findings describe shared biological effects of cycle-one therapy rather than response-discriminating features.

Previous spatial imaging work in breast cancer has been predominantly conducted on static, single-time-point tissue, classifying baseline TNBC architecture into prognostic categories such as mixed versus compartmentalised [14] and identifying distinct immune organisations using imaging mass cytometry [15, 16]. The NeoTRIP study extended this paradigm by profiling longitudinal TNBC tissue during neoadjuvant checkpoint blockade using a high-dimensional imaging mass cytometry panel [13]. Our study evaluates an earlier post-cycle-1 timepoint and applies a six-colour mIF panel that may be more readily implemented in pathology laboratories. These findings therefore complement high-dimensional imaging studies by testing whether early spatial reorganisation can be detected with a lower-plex workflow.

These findings should be interpreted within the constraints of an exploratory single-centre design. With n = 10 patients (five per response group) and no formal sample-size calculation for these exploratory spatial endpoints, statistical precision is limited, particularly for between-group effect sizes and the exploratory ROC estimate. Of the 48 tests evaluated under the tier-specific BH-FDR framework, four cohort-wide signals survived BH-FDR at $q < 0.05$ (detailed in Results); the post-treatment Sintra/immune difference ($q = 0.064$) and the peritumoral CD20+–FOXP3 + Δ comparison ($q = 0.256$) did not, and are reported as hypothesis-generating. Four further constraints follow from the same exploratory design. First, the six-colour panel was sufficient for the spatial architecture questions addressed here but precluded functional subtyping of macrophage polarisation, B cell maturation, and T cell exhaustion; in particular, the mechanistic interpretation of the IH_{intra} CD68+–FOXP3 + decrease via the TAM–Treg axis is M2-specific and will require CD163 or CD206 co-staining to test directly. Second, core-needle biopsies and a uniform single-centre regimen limit generalisability and may not fully capture intra-tumour heterogeneity. Third, although pCR is an approval-enabling surrogate endpoint, its relationship with long-term outcomes is subtype- and patient-dependent [28], and longer follow-up will be required to link cycle-one spatial signals with event-free survival. Fourth, the regimen comprised three concurrent active components — sintilimab, anlotinib (a multi-target VEGFR/PDGFR/FGFR inhibitor), and chemotherapy — each with documented capacity to remodel the tumour microenvironment, including checkpoint relief, anti-angiogenic vascular normalisation with concomitant myeloid reprogramming, and immunogenic cell death; the present design therefore characterises the integrated cycle-one tumour immune microenvironment response without disentangling the individual contribution of each agent. Together, these considerations frame the present results as hypothesis-generating signals that warrant prospective validation in larger, multi-centre cohorts with expanded marker panels and extended follow-up.

Conclusions

Cycle-one multi-layer spatial profiling identified early reorganisation of the TNBC immune microenvironment within the first three weeks of neoadjuvant combination therapy, including hotspot-level features associated with subsequent pathological response at the exploratory level. These findings require prospective validation in larger cohorts before early spatial features can be considered for treatment-adaptation strategies.

Abbreviations

AUC
area under the receiver operating characteristic curve
BH-FDR
Benjamini–Hochberg false discovery rate
C1
post-cycle 1
CSR
complete spatial randomness
FFPE
formalin-fixed paraffin-embedded
IF
immunofluorescence
IHC
immunohistochemistry
IH_{intra}
intratumoral immune hotspot
IH_{peri}
peritumoral immune hotspot
mIF
multiplex immunofluorescence
PANCK
pan-cytokeratin
pCR
pathological complete response
ROC
receiver operating characteristic
TLS
tertiary lymphoid structure
TNBC
triple-negative breast cancer

Treg
regulatory T cell.

Declarations

Ethics approval and consent to participate

The parent NeoSACT trial was approved by the Research Ethics Committee of Guangdong General Hospital, Guangdong Academy of Medical Sciences (approval no. KY-Z-2021-511-01). The trial was prospectively registered at ClinicalTrials.gov (NCT04877821; first submitted on 30 April 2021 and first posted on 7 May 2021). All participants provided written informed consent for trial participation and the use of collected biospecimens for research in accordance with the Declaration of Helsinki.

Consent for publication

Not applicable.

Competing interests

The authors declare no competing interests.

Funding

This study did not receive any specific grant or external funding.

Author Contribution

Jiao-mei Yuan, Kun Wang and Fei Ji designed the study. Jiao-mei Yuan performed the spatial and statistical analyses and drafted the manuscript. Kun Wang and Fei Ji provided clinical oversight, supervised the study, and critically revised the manuscript. All authors interpreted the data, read and approved the final manuscript.

Acknowledgement

The authors thank all patients who participated in the parent clinical trial and consented to the use of their biopsy specimens for research purposes.

Data Availability

The datasets generated and analysed during the current study are not publicly available due to patient privacy considerations but are available from the corresponding author upon reasonable request. The custom R code used for the multi-layer spatial analyses is also available from the corresponding author upon reasonable request.

References

1. Sung, H. et al. Global cancer statistics 2020: GLOBOCAN estimates of incidence and mortality worldwide for 36 cancers in 185 countries. *CA Cancer J. Clin.* **71**, 209–249 (2021).
2. Bianchini, G., Balko, J. M., Mayer, I. A., Sanders, M. E. & Gianni, L. Triple-negative breast cancer: challenges and opportunities of a heterogeneous disease. *Nat. Rev. Clin. Oncol.* **13**, 674–690 (2016).
3. Foulkes, W. D., Smith, I. E. & Reis-Filho, J. S. Triple-negative breast cancer. *N Engl. J. Med.* **363**, 1938–1948 (2010).
4. Schmid, P. et al. Pembrolizumab for early triple-negative breast cancer. *N Engl. J. Med.* **382**, 810–821 (2020).
5. Schmid, P. et al. Event-free survival with pembrolizumab in early triple-negative breast cancer. *N Engl. J. Med.* **386**, 556–567 (2022).
6. Mittendorf, E. A. et al. Neoadjuvant atezolizumab in combination with sequential nab-paclitaxel and anthracycline-based chemotherapy versus placebo and chemotherapy in patients with early-stage triple-negative breast cancer (IMpassion031): a randomised, double-blind trial. *Lancet* **396**, 1090–1100 (2020).
7. Loibl, S. et al. A randomised phase II study investigating durvalumab in addition to an anthracycline taxane-based neoadjuvant therapy in early triple-negative breast cancer: clinical results and biomarker analysis of GeparNuevo study. *Ann. Oncol.* **30**, 1279–1288 (2019).
8. Denkert, C. et al. Tumour-infiltrating lymphocytes and prognosis in different subtypes of breast cancer: a pooled analysis of 3771 patients treated with neoadjuvant therapy. *Lancet Oncol.* **19**, 40–50 (2018).
9. Ji, F. et al. Tumor microenvironment characterization in breast cancer identifies prognostic and neoadjuvant chemotherapy relevant signatures. *Front. Mol. Biosci.* **8**, 759495 (2021).
10. Heindl, A. et al. Relevance of spatial heterogeneity of immune infiltration for predicting risk of recurrence after endocrine therapy of ER+ breast cancer. *J. Natl. Cancer Inst.* **110**, djx137 (2018).
11. Nawaz, S., Heindl, A., Koelble, K. & Yuan, Y. Beyond immune density: critical role of spatial heterogeneity in estrogen receptor-negative breast cancer. *Mod. Pathol.* **28**, 766–777 (2015).
12. Heindl, A., Nawaz, S. & Yuan, Y. Mapping spatial heterogeneity in the tumor microenvironment: a new era for digital pathology. *Lab. Invest.* **95**, 377–384 (2015).
13. Wang, X. Q. et al. Spatial predictors of immunotherapy response in triple-negative breast cancer. *Nature* **621**, 868–876 (2023).

14. Keren, L. et al. A structured tumor-immune microenvironment in triple negative breast cancer revealed by multiplexed ion beam imaging. *Cell* **174**, 1373–1387e19 (2018).
15. Jackson, H. W. et al. The single-cell pathology landscape of breast cancer. *Nature* **578**, 615–620 (2020).
16. Danenberg, E. et al. Breast tumor microenvironment structures are associated with genomic features and clinical outcome. *Nat. Genet.* **54**, 660–669 (2022).
17. Gruosso, T. et al. Spatially distinct tumor immune microenvironments stratify triple-negative breast cancers. *J. Clin. Invest.* **129**, 1785–1800 (2019).
18. Sanchez, K. et al. Multiplex immunofluorescence to measure dynamic changes in tumor-infiltrating lymphocytes and PD-L1 in early-stage breast cancer. *Breast Cancer Res.* **23**, 2 (2021).
19. Dieu-Nosjean, M. C. et al. Tertiary lymphoid structures, drivers of the anti-tumor responses in human cancers. *Immunol. Rev.* **271**, 260–275 (2016).
20. Cabrita, R. et al. Tertiary lymphoid structures improve immunotherapy and survival in melanoma. *Nature* **577**, 561–565 (2020).
21. Helmink, B. A. et al. B cells and tertiary lymphoid structures promote immunotherapy response. *Nature* **577**, 549–555 (2020).
22. Sautès-Fridman, C., Petitprez, F., Calderaro, J. & Fridman, W. H. Tertiary lymphoid structures in the era of cancer immunotherapy. *Nat. Rev. Cancer*. **19**, 307–325 (2019).
23. Zhang, H. et al. Spatial positioning of immune hotspots reflects the interplay between B and T cells in lung squamous cell carcinoma. *Cancer Res.* **83**, 1410–1425 (2023).
24. Qian, B. Z. & Pollard, J. W. Macrophage diversity enhances tumor progression and metastasis. *Cell* **141**, 39–51 (2010).
25. DeNardo, D. G. & Ruffell, B. Macrophages as regulators of tumour immunity and immunotherapy. *Nat. Rev. Immunol.* **19**, 369–382 (2019).
26. Curiel, T. J. et al. Specific recruitment of regulatory T cells in ovarian carcinoma fosters immune privilege and predicts reduced survival. *Nat. Med.* **10**, 942–949 (2004).
27. Mantovani, A., Allavena, P., Marchesi, F. & Garlanda, C. Macrophages as tools and targets in cancer therapy. *Nat. Rev. Drug Discov*. **21**, 799–820 (2022).
28. Cortazar, P. et al. Pathological complete response and long-term clinical benefit in breast cancer: the CTNeoBC pooled analysis. *Lancet* **384**, 164–172 (2014).
29. Taube, J. M. et al. The Society for Immunotherapy of Cancer statement on best practices for multiplex immunohistochemistry (IHC) and immunofluorescence (IF) staining and validation. *J. Immunother Cancer*. **8**, e000155 (2020).
30. Peranzoni, E. et al. Macrophages impede CD8 T cells from reaching tumor cells and limit the efficacy of anti-PD-1 treatment. *Proc. Natl. Acad. Sci. U S A*. **115**, E4041–E4050 (2018).

Figures

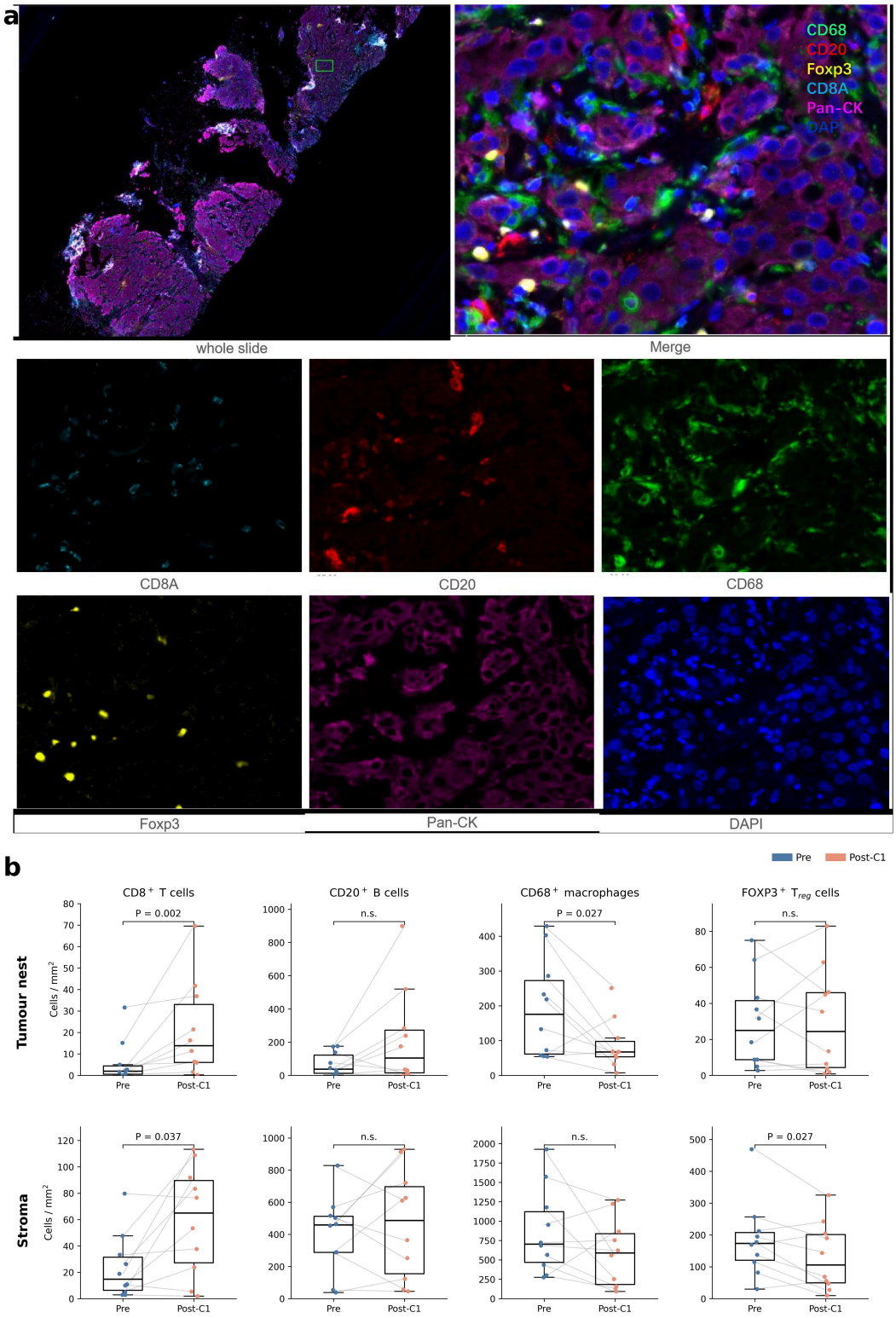


Figure 1

Multiplex immunofluorescence staining and immune cell density analysis before and after a single cycle of neoadjuvant combination therapy. a Representative six-colour multiplex immunofluorescence staining of a pre-treatment core-needle biopsy. Upper row: whole-slide overview (left) and merged image from the region indicated (right), showing CD68 (green), CD20 (red), FOXP3 (yellow), CD8A (cyan), pan-cytokeratin (magenta), and DAPI (blue). Middle and lower rows: individual marker channels of the same region. b

Immune cell density in the tumour nest (upper) and stroma (lower) before (blue) and after one cycle of treatment (orange; n = 10). Each dot represents one patient; grey lines connect matched pre- and post-treatment samples. P values: two-sided Wilcoxon signed-rank test; n.s., P ≥ 0.10.

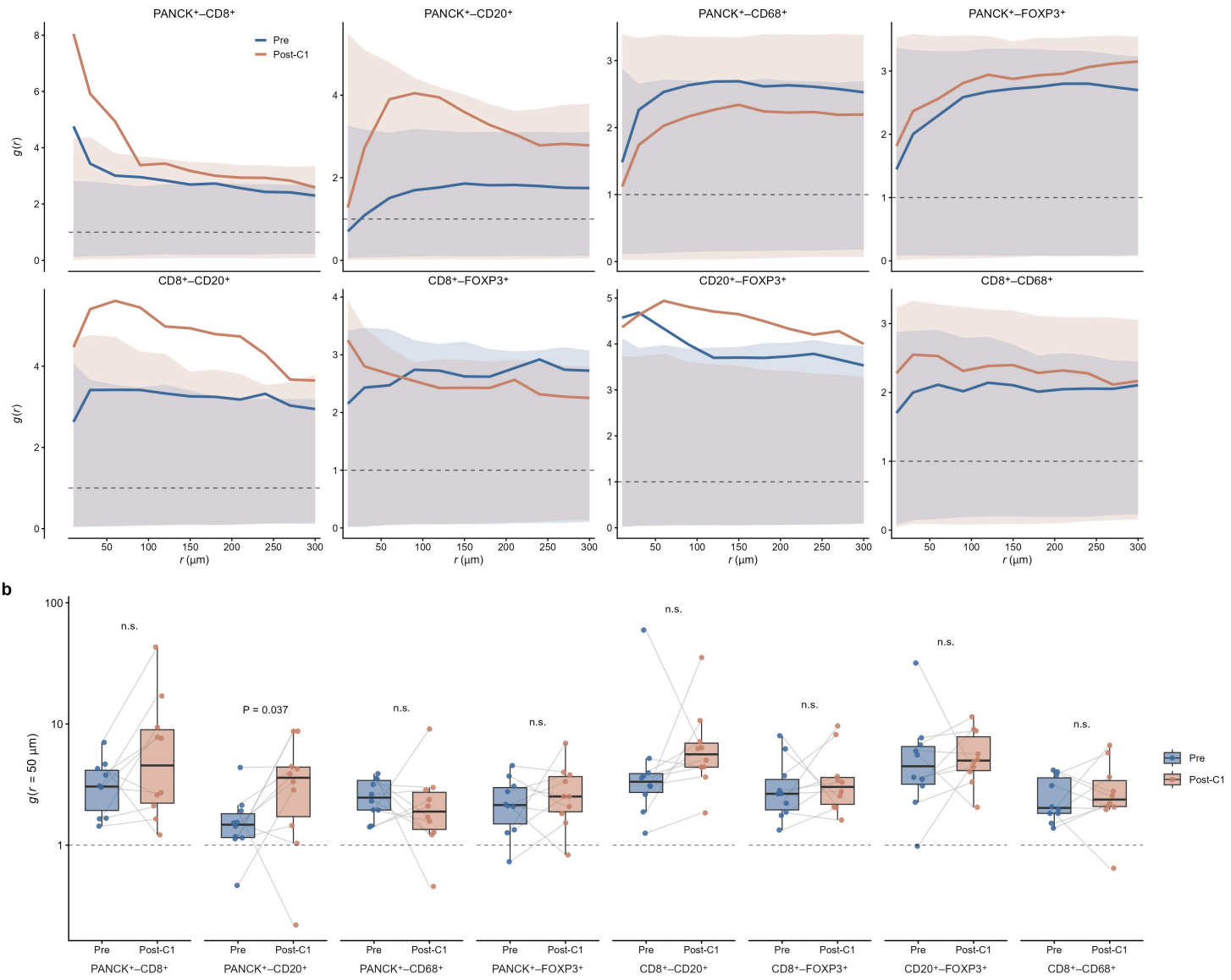


Figure 2

Bivariate cross-pair correlation function (cross-PCF) analysis of spatial co-localisation between immune and tumour cell pairs. a Cross-PCF curves (g(r)) for eight cell pairs — four tumour–immune pairs (PANCK+ as reference, upper) and four immune–immune pairs (lower). Bold lines indicate the median across patients (blue, pre-treatment; orange, post-treatment C1; n = 10 each). Shaded bands indicate the 95% complete spatial randomness (CSR) envelope (median across samples; light blue, pre; light orange, post). The dotted horizontal line marks g(r) = 1; values above indicate spatial co-localisation. b g(r) values at r = 50 μm for all eight cell pairs (n = 10 paired). P values: two-sided Wilcoxon signed-rank test; n.s., P ≥ 0.10.

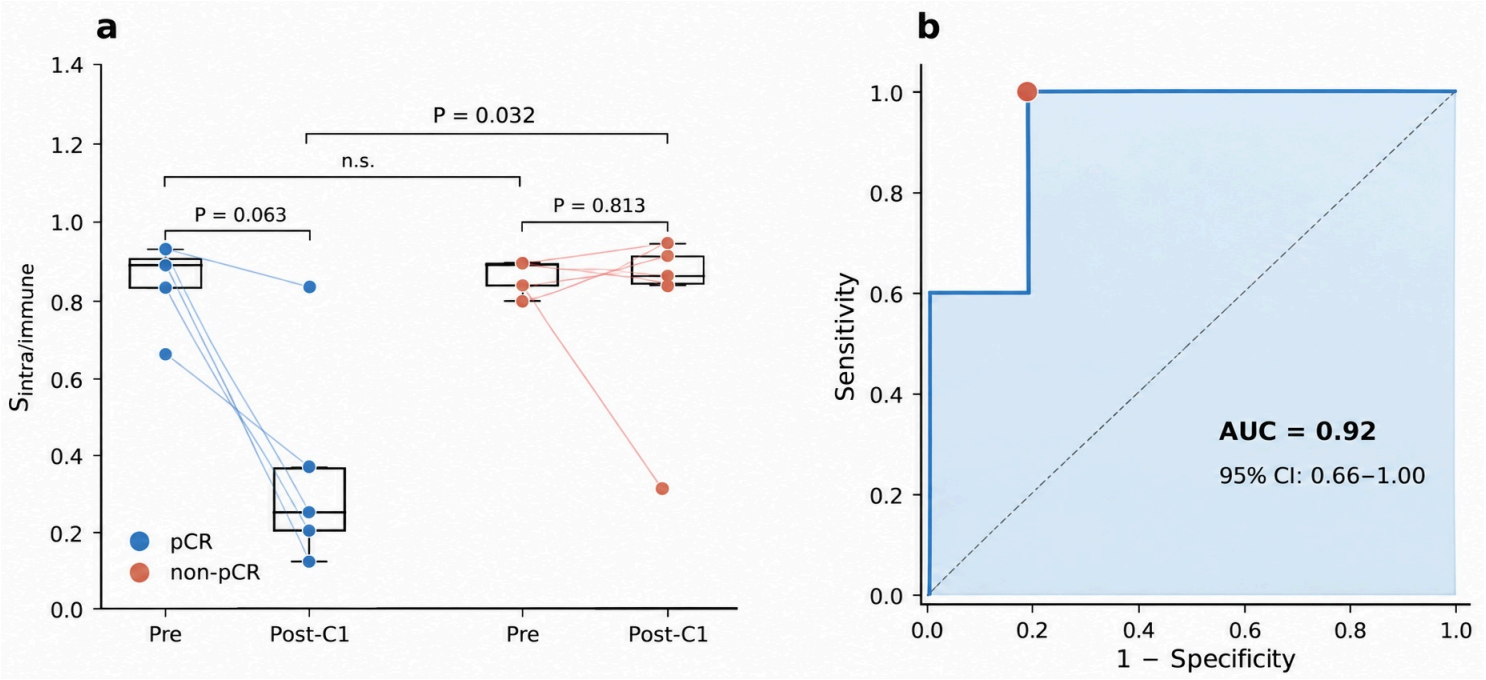


Figure 3

Changes in the intratumoral immune hotspot score (Sintra/immune) and its association with pathological response. a, Pre- versus post-cycle-1 comparison of Sintra/immune stratified by response group (pCR, blue; non-pCR, orange; n = 5 per group). Lines connect matched pre- and post-treatment samples. Short brackets indicate within-group pre- versus post-treatment comparisons; the long bracket indicates the post-treatment between-group comparison. P values were calculated using the two-sided Wilcoxon signed-rank test for within-group comparisons and the two-sided Mann–Whitney U test for between-group comparisons; n.s., P ≥ 0.10.
b, Exploratory receiver operating characteristic (ROC) curve illustrating the separation of pCR and non-pCR patients by post-treatment Sintra/immune. The area under the curve (AUC) and 95% bootstrap confidence interval are shown.

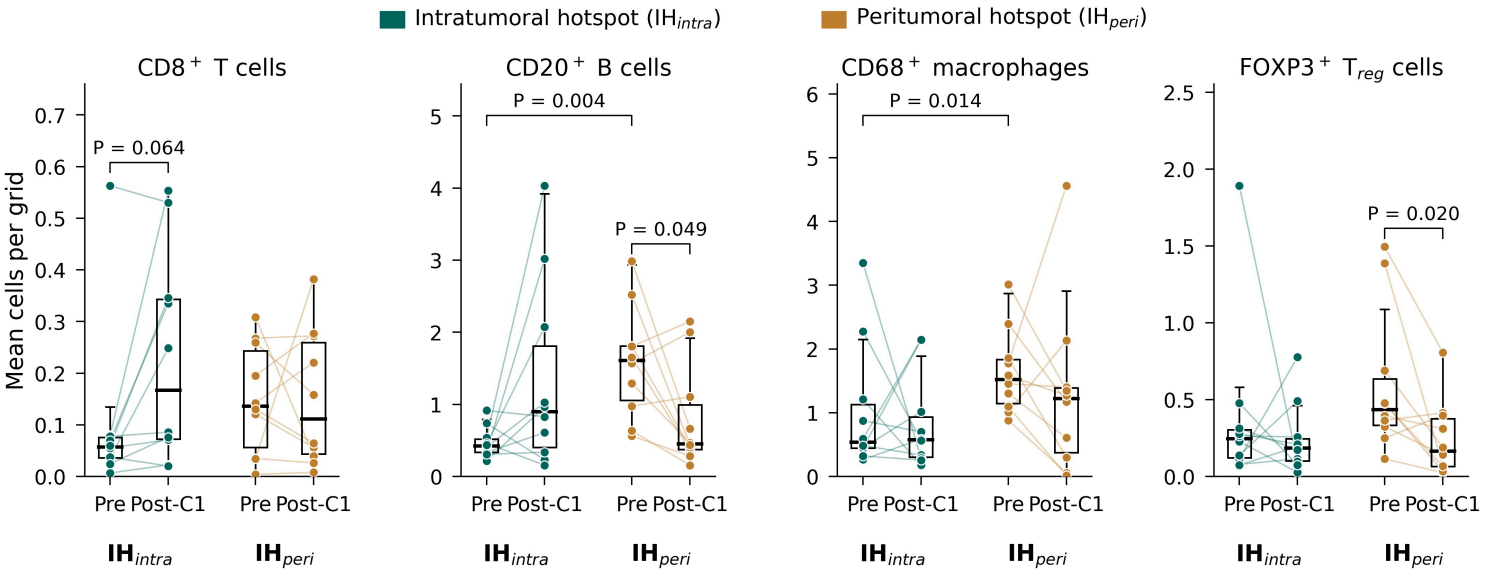


Figure 4

Immune cell density within intratumoral (IH_{intra}, dark teal) and peritumoral (IH_{peri}, dark goldenrod) immune hotspot compartments before and after neoadjuvant combination therapy. Each dot represents one patient (n = 10 paired); lines connect matched pre- and post-treatment samples. Short brackets indicate pre- versus post-treatment comparisons within each compartment; long brackets indicate IH_{intra} versus IH_{peri} comparisons at baseline (pre-treatment). Only P values below 0.10 are annotated; non-annotated comparisons did not reach this threshold. Two-sided Wilcoxon signed-rank test.

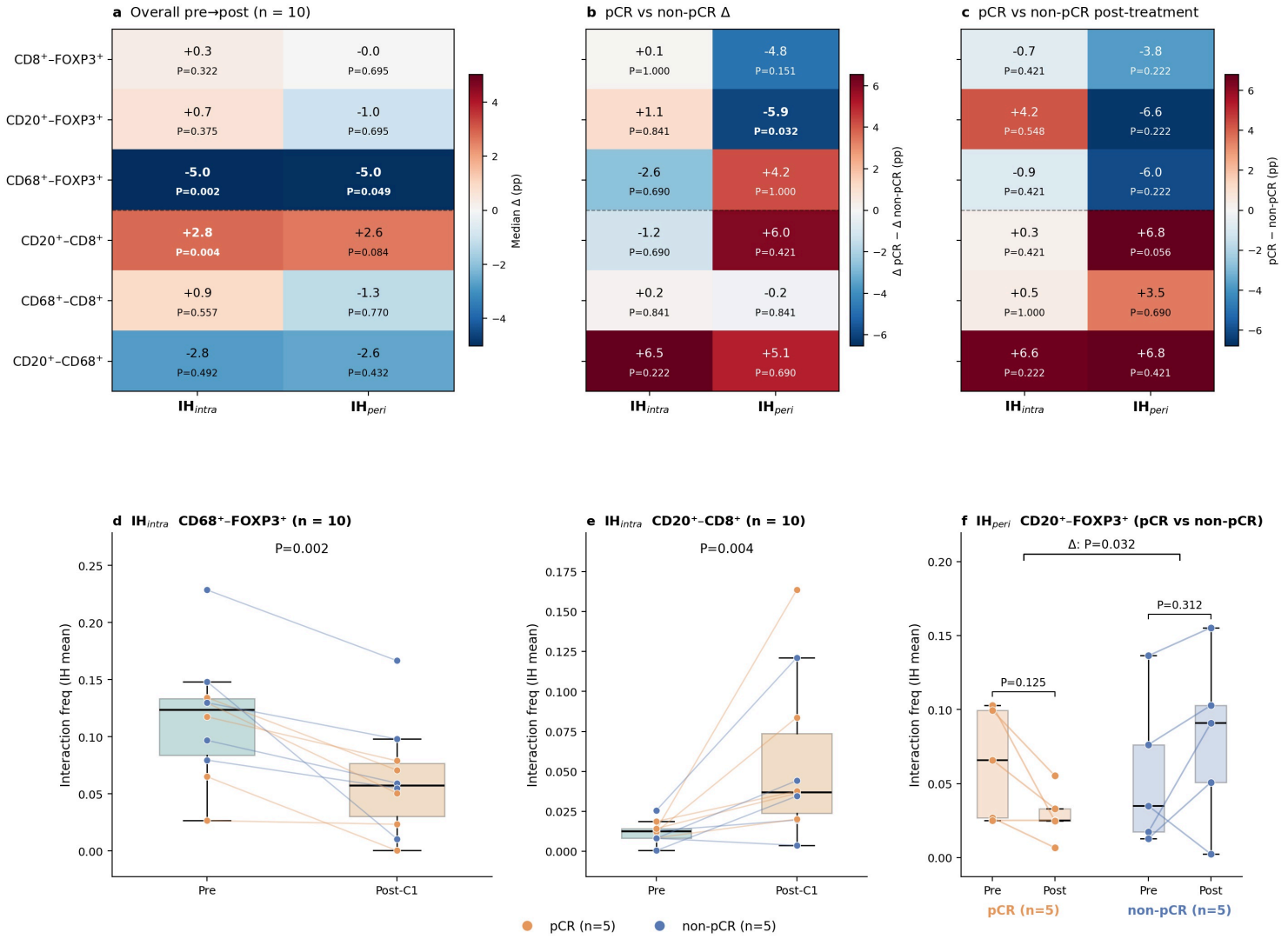


Figure 5

Delaunay triangulation-based analysis of within-hotspot immune cell interactions. a Heatmap of the median within-patient change (Δ, in percentage points) between pre-treatment and post-cycle 1 for six immune cell-cell pairs in IH_{intra} and IH_{peri} hotspots (n = 10 paired; two-sided Wilcoxon signed-rank test). b Heatmap of the median Δ difference (pCR minus non-pCR) for the same 12 pair × compartment combinations (two-sided Mann–Whitney U test). c Heatmap of the median post-treatment difference

(pCR minus non-pCR) for absolute-value comparisons of interaction frequencies (two-sided Mann–Whitney U test). In all heatmaps (a–c), each cell shows the median value (top) and the raw P value (bottom); colour intensity indicates the magnitude of the median value, and the dashed horizontal line separates FOXP3+-involving pairs (upper rows) from non-FOXP3+ pairs (lower rows). In panels d–f, individual data points are coloured by response group (pCR, orange; non-pCR, blue; n = 5 per group). d Paired pre versus post-cycle 1 comparison of IH_{intra} CD68+–FOXP3+ interaction frequency. e Paired pre versus post-cycle 1 comparison of IH_{intra} CD20+–CD8+ interaction frequency. f IH_{peri} CD20+–FOXP3+ interaction frequency in pCR (left) and non-pCR (right) groups, with pre and post shown for each group. Within-group P values (pre vs post; two-sided Wilcoxon signed-rank test) and the between-group Δ P value (Δ = post − pre, pCR vs non-pCR; two-sided Mann–Whitney U test) are annotated on the plot.

Supplementary Files

This is a list of supplementary files associated with this preprint. Click to download.

- SupplementaryTableS1.docx
- SupplementaryTableS2.docx
- SupplementaryTableS4.docx
- SupplementaryTableS5.xlsx
- SupplementaryTableS6.docx